Monthly Notices
of the
ROYAL ASTRONOMICAL SOCIETY

MNRAS **493,** 1531–1545 (2020)
Advance Access publication 2020 January 28

doi:10.1093/mnras/staa229

ExoMol molecular line lists – XXXVII. Spectra of acetylene

Katy L. Chubb,[1,2] Jonathan Tennyson[1]★ and Sergei N. Yurchenko[1]

[1]*Department of Physics and Astronomy, University College London, London WC1E 6BT, UK*
[2]*SRON Netherlands Institute for Space Research, Sorbonnelaan 2, Utrecht NL-3584 CA, the Netherlands*

Accepted 2020 January 7. Received 2019 December 28; in original form 2019 November 16

ABSTRACT

A new ro-vibrational line list for the ground electronic state of the main isotopologue of acetylene, $^{12}C_2H_2$, is computed as part of the ExoMol project. The aCeTY line list covers the transition wavenumbers up to 10 000 cm^{-1} ($\lambda > 1$ μm), with lower and upper energy levels up to 12 000 and 22 000 cm^{-1} considered, respectively. The calculations are performed up to a maximum value for the vibrational angular momentum, $K_{max} = L_{max} = 16$, and maximum rotational angular momentum, $J = 99$. Higher values of J were not within the specified wavenumber window. The aCeTY line list is considered to be complete up to 2200 K, making it suitable for use in characterizing high-temperature exoplanet or cool stellar atmospheres. Einstein-A coefficients, which can directly be used to calculate intensities at a particular temperature, are computed for 4.3 billion (4 347 381 911) transitions between 5 million (5 160 803) energy levels. We make comparisons against other available data for $^{12}C_2H_2$, and demonstrate this to be the most complete line list available. The line list is available in electronic form from the online CDS and ExoMol data bases.

Key words: molecular data – planets and Satellites: atmospheres – stars: atmosphere – stars: carbon.

1 INTRODUCTION

In its electronic ground state, acetylene, HCCH, is a linear tetratomic unsaturated hydrocarbon whose spectra is important in a large range of environments. On the Earth, these range from the hot, monitoring of oxy-acetylene flames that are widely used for welding and related activities (Schmidt et al. 2010; Gaydon 2012), to the temperate, monitoring of acetylene in breath, giving insights into the nature of exhaled smoke (Metsälä et al. 2010), vehicle exhausts (Schmidt et al. 2010), and other air-born pollutants (Hughes & Gorden 1959). Acetylene is also important in the production of synthetic diamonds using carbon-rich plasma (Kelly et al. 2012).

Further out in our Solar system, acetylene is found in the atmospheres of cold gas giants Saturn (de Graauw et al. 1997; Moses et al. 2000), Uranus (Encrenaz et al. 1986), and Jupiter (Ridgway 1974; Drossart et al. 1986), the hydrothermal plumes of Enceladus (Waite et al. 2006; Miller, Baesman & Oremland 2014), and in the remarkably early Earth-like atmosphere of Titan (Oremland & Voytek 2008; Singh et al. 2016; Hörst 2017; Dinelli et al. 2019), where there has even been some speculation as to acetylene's role in potential non-earth-like life (Belay & Daniels 1987; Bains 2004; McKay & Smith 2005; Oremland & Voytek 2008; Lovett 2011; Seager, Bains & Hu 2013) and reactions involving molecules of pre-biotic interest (Oremland & Voytek 2008; Lovett 2011; Hörst 2017). It has been detected on comets such as Hyakotake (Brooke et al. 1996), Halley, and 67P/Churyumov–Gerasimenko (Le Roy et al. 2015). Even further into the Galactic neighbourhood, acetylene appears in star-forming regions (Ridgway et al. 1976; van Dishoeck et al. 1998; Rangwala et al. 2018), is speculated to be an important constituent of clouds in the upper atmospheres of brown dwarfs and exoplanets (Shabram et al. 2011; Bilger, Rimmer & Helling 2013; Oppenheimer et al. 2013; Madhusudhan et al. 2016; Tennyson & Yurchenko 2016, 2017), and is thought to play an important role in dust formation (Dhanoa & Rawlings 2014) and asymptotic giant branch star evolution and atmospheric composition (Loidl et al. 1999; Jørgensen, Hron & Loidl 2000; Cernicharo 2004; Gautschy-Loidl et al. 2004; Aringer et al. 2009), providing a major source of opacity in cool carbon stars (Rinsland, Baldacci & Rao 1982; Gautschy-Loidl et al. 2004). For example, C_2H_2 was detected in the carbon star Y CVn by Goebel et al. (1978) and in the low-mass young stellar object IRS 46 by Lahuis et al. (2005). The first analysis of the atmosphere of a 'super-Earth' exoplanet, 55 Cancri e by Tsiaras et al. (2016), speculates that acetylene could be present in its atmosphere; however, the spectral data available at the time did not allow for an accurate verification of its presence in such a high-temperature environment. A similar conclusion was found for the 'hot Jupiter' extrasolar planet HD 189733b (de Kok et al. 2014) and for carbon-rich stars in the Large Magellanic Cloud (Matsuura et al. 2006; Lederer & Aringer 2009; Marigo & Aringer 2009).

★ E-mail: j.tennyson@ucl.ac.uk

Table 1. Quantum numbers used to classify the energy states of acetylene, $^{12}C_2H_2$.

Label	Description
	Conventional (normal mode) quantum numbers
υ_1	CH symmetric stretch (Σ_g^+)
υ_2	CC symmetric stretch (Σ_g^+)
υ_3	CH antisymmetric stretch (Σ_u^+)
υ_4	Symmetric (trans) bend (Π_g)
ℓ_4	Vibrational angular momentum associated with υ_4
υ_5	Antisymmetric (cis) bend (Π_u)
ℓ_5	Vibrational angular momentum associated with υ_5
$L = \lvert l \rvert$	Total vibrational angular momentum, $\lvert \ell_4 + \ell_5 \rvert$
$K = \lvert k \rvert$	Rotational quantum number; z-projection of $\boldsymbol{J}$
J	QN associated with rotational angular momentum, $\boldsymbol{J}$.
e/f	Rotationless parity of the ro-vibrational state
Ortho/para	Nuclear spin state, see Chubb, Jensen & Yurchenko (2018a)
	TROVE local mode quantum numbers
n_1	CC symmetric stretch
n_2	CH_1 stretch
n_3	CH_2 stretch
n_4	x_1 bend
n_5	y_1 bend
n_6	x_2 bend
n_7	y_2 bend
$L = \lvert l \rvert$	Total vibrational angular momentum $L = K$
$\Gamma_{\rm str}$	Symmetry of the vibrational component ($\mathcal{D}_{nh}$, $n = 34$)
$K = \lvert k \rvert$	Rotational quantum number; z-projection of $\boldsymbol{J}$
$\Gamma_{\rm rot}$	Symmetry of the rotational component ($\mathcal{D}_{nh}$, $n = 34$)
J	QN associated with rotational angular momentum, $\boldsymbol{J}$.
$\Gamma_{\rm tot}$	Symmetry of the rotational component ($\mathcal{D}_{nh}$, $n = 34$)

The infrared spectrum of acetylene has been well studied in the laboratory, see Amyay et al. (2016) and Lyulin & Campargue (2017), for example; a complete, up to 2017, compilation of laboratory studies can be found in Chubb et al. (2018c). More recent studies include those of Lyulin & Campargue (2018), Cassady, Peng & Hanson (2018), and Lyulin et al. (2018, 2019).

At the temperatures of many exoplanets and cool stars (up to around 3000–4000 K; Tanaka et al. 2007; Gaudi et al. 2017), molecules are expected in abundance (Tsuji 1986). An essential component in the analysis of such astrophysical atmospheres is therefore accurate and comprehensive spectroscopic data for all molecules of astrophysical importance, for a variety of pressures and temperatures. While a large amount of highly accurate data have been determined experimentally for a number of such molecules, they have largely been measured at room temperature and are thus not well suited to the modelling of high-temperature environments; theoretical data are required for this purpose. The ExoMol project (Tennyson & Yurchenko 2012; Tennyson et al. 2016) was set up for this reason, to produce a data base of computed line lists appropriate for modelling exoplanet, brown dwarf, or cool stellar atmospheres. As a result, high-quality variational line lists that are appropriate up to high temperatures have been computed for a host of molecules as part of the ExoMol project, including CH_4 (Yurchenko & Tennyson 2014; Yurchenko et al. 2014, 2017b), HCN/HNC (Barber et al. 2014), NH_3 (Coles et al. 2019), PH_3 (Sousa-Silva et al. 2015), H_2O_2 (Al-Refaie et al. 2016), SO_2 (Underwood et al. 2016a), H_2S (Azzam et al. 2016), SO_3 (Underwood et al. 2016b), VO (McKemmish, Yurchenko & Tennyson 2016), CO_2 (Zak et al. 2017), SiH_4 (Owens et al. 2017), H_2O (Polyansky et al. 2017), C_2H_4 (Mant et al. 2018), and, as presented in this work, C_2H_2 (see also Chubb et al. 2018b). Other molecular spectroscopic data bases include HITRAN (Rothman et al. 2010a), HITEMP (Rothman et al. 2010b), CDMS (Endres et al. 2016), GEISA (Jacquinet-Husson et al. 2016), TheoReTS (Rey et al. 2016), SPECTRA (Mikhailenko, Babikov & F. 2005), PNNL (Sharpe et al. 2004), MeCaSDA, and ECaSDa (Ba et al. 2013); however, none of these provide line lists for hot acetylene. The ASD-1000 data base of Lyulin & Perevalov (2017) provides data on acetylene transitions that is designed to be valid for temperatures up to 1000 K; we compare with this data base next.

Acetylene is a four-atomic (tetratomic) molecule that is linear in its equilibrium configuration. The rotation–vibration spectrum of a polyatomic molecule of this size, at the temperatures of exoplanets and cool stars, typically spans the infrared region of the electromagnetic spectrum. In this region, only transitions between rotation–vibration (ro-vibrational) levels are important; electronic transitions are of too high energy to be of interest. Such ro-vibrational calculations essentially require a solution to the nuclear-motion Schrödinger equation, with some approximations required to enable feasible computational treatment. The challenge with acetylene comes with its linear geometry at equilibrium structure; linear molecules require special consideration for calculations of ro-vibrational energies. This was demonstrated by Watson (1968) and very recently by Chubb et al. (2018b); these two approaches differ in their choice of internal coordinates used to represent the vibrational Hamiltonian.

This paper is structured as follows. In Section 2, we outline the details of the calculations used to produce the aCeTY line list. This Section includes details on the basis set in Section 2.1, the potential energy surface (PES) in Section 2.2, the refinement of this surface to empirical energy levels in Section 2.3, empirical band centre replacement in Section 2.4, and details of the dipole moment surface (DMS) and its subsequent scaling in Sections 2.5 and 2.6, respectively. The results of the line list calculations are given in Section 3, with comparisons of the resulting spectra made against previous works in Section 4. In Section 5, we demonstrate the differences in applying different line list data to exoplanet atmosphere modelling. We give our summary in Section 6.

2 CALCULATIONS

The $(3N - 5)$ model for treating a *N=4* atomic linear molecule such as HCCH has been fully implemented in the variational nuclear motion program THEORETICAL ROVIBRATIONAL ENERGIES (TROVE; Yurchenko, Thiel & Jensen 2007; Yachmenev & Yurchenko 2015; Yurchenko, Yachmenev & Ovsyannikov 2017a), as detailed in Chubb et al. (2018b). Here, we outline only the main calculation steps towards computing the extensive aCeTY ro-vibrational line list for C_2H_2 in its ground electronic state.

2.1 Basis set

The polyad number used to control the size of the primitive and contracted basis sets is given by

$$P = 2n_1 + n_2 + n_3 + n_4 + n_5 + n_6 + n_7 \leq P_{\rm max}. \quad (1)$$

Here, the vibrational quantum numbers (QNs) follows the TROVE basis set selection, with n_1 corresponding to the excitation of the C–C stretching mode, n_2 and n_3 representing the C–H_1 and C–H_2 stretching modes and n_4, n_5, n_6, and n_7 representing the bending modes (see Table 1). This local mode notation deviates from the standard normal mode QNs used for $^{12}C_2H_2$, most notedly for the bending modes: the TROVE bending QNs n_4, n_5, n_6, n_7 represent

Table 2. An extract of the Obs.-Calc. residuals for $^{12}C_2H_2$. The root-mean-square errors between the experimental and calculated (refined) ro-vibrational energies for different vibrational bands (classified by their symmetry Γ, quantum numbers υ_1, υ_2, υ_3, υ_4, l_4, υ_5, l_5, k, and energy E_i/hc), before (rms-I) and after (rms-II) the band centre shifts. The full table is given as part of the supplementary information to this paper. E_i/hc is the TROVE energy after the band centre shift.

Γ	υ_1	υ_2	υ_3	υ_4	l_4	υ_5	l_5	k	E_i/hc	rms-I	rms-II
Σ_g^+	0	0	0	0	0	0	0	0	0.00	0.0009	0.0009
Π_g	0	0	0	1	1	0	0	1	612.86	0.0021	0.0021
Π_u	0	0	0	0	0	1	1	1	730.33	0.0016	0.0016
Σ_g^+	0	0	0	2	0	0	0	0	1230.38	0.0160	0.0042
Δ_g	0	0	0	2	2	0	0	2	1233.49	0.0151	0.0137
Σ_u^+	0	0	0	1	1	1	−1	0	1328.07	0.2978	0.0012
Σ_u^-	0	0	0	1	1	1	−1	0	1340.55	0.0045	0.0017
Δ_u	0	0	0	1	1	1	1	2	1347.51	0.0048	0.0048
Σ_g^+	0	0	0	0	0	2	0	0	1449.11	0.0043	0.0012
Δ_g	0	0	0	0	0	2	2	2	1463.00	0.0082	0.0081
Π_g	0	0	0	3	1	0	0	1	1855.77	0.0548	0.0037
Π_u	0	0	0	2	2	1	−1	1	1941.18	0.3933	0.0019
Π_u	0	0	0	2	0	1	1	1	1960.87	0.0024	0.0023
Σ_g^+	0	1	0	0	0	0	0	0	1974.35	0.0242	0.0185
Π_g	0	0	0	1	1	2	0	1	2049.06	0.0298	0.0021
Π_g	0	0	0	1	−1	2	2	1	2066.97	0.0394	0.0031
Φ_g	0	0	0	1	1	2	2	3	2084.68	0.0708	0.0698
Π_u	0	0	0	0	0	3	1	1	2170.34	0.1247	0.0005
Σ_u^+	0	0	0	3	1	1	−1	0	2560.59	0.1499	0.0027
Π_g	0	1	0	1	1	0	0	1	2574.76	0.2551	0.0193
Σ_u^-	0	0	0	3	1	1	−1	0	2583.84	0.6489	0.0043
Σ_g^+	0	0	0	2	2	2	−2	0	2648.01	0.0233	0.0058
Σ_g^-	0	0	0	2	2	2	−2	0	2661.16	0.1688	0.0088
Δ_g	0	0	0	2	2	2	0	2	2666.06	0.5931	0.0009
Π_u	0	1	0	0	0	1	1	1	2703.10	0.0073	0.0072
Σ_u^+	0	0	0	1	1	3	−1	0	2757.80	0.0314	0.0011
Σ_g^+	0	0	0	0	0	4	0	0	2880.22	0.1967	0.0025
Δ_g	0	0	0	0	0	4	2	2	2894.04	0.0195	0.0161
Σ_u^+	0	1	0	1	1	1	−1	0	3281.91	0.0040	0.0040
Σ_u^+	0	0	1	0	0	0	0	0	3294.85	0.0112	0.0039
Σ_u^-	0	1	0	1	1	1	−1	0	3300.65	0.0802	0.0078
Δ_u	0	1	0	1	1	1	1	2	3307.73	0.2140	0.0023
Σ_g^+	1	0	0	0	0	0	0	0	3372.84	0.1657	0.0028
Π_u	0	1	0	2	0	1	1	1	3882.42	0.9276	0.0032
Π_u	0	0	1	1	1	0	0	1	3898.34	0.0481	0.0017
Σ_g^+	0	2	0	0	0	0	0	0	3933.97	0.0387	0.0297
Π_g	1	0	0	1	1	0	0	1	3970.05	0.0097	0.0043
Π_g	0	1	0	1	1	2	0	1	4002.46	0.0396	0.0076
Π_g	0	0	1	0	0	1	1	1	4016.73	0.0979	0.0056
Π_u	1	0	0	0	0	1	1	1	4092.34	0.0558	0.0011
Π_u	0	1	0	0	0	3	1	1	4140.08	0.7091	0.0084

excitations along the Δx_1, Δy_1, Δx_2, Δy_2, respectively, while the corresponding normal mode QNs correspond to symmetric (υ_4) and asymmetric (υ_5) modes as well as to the corresponding vibrational angular momenta (ℓ_4 and ℓ_5), see Table 1 and also Section 3.

For a linear molecule such as HCCH, another condition has been introduced in TROVE to control the basis set size; a maximum value for the total vibrational angular momentum, $L_{\max}$, which is equal to the z-projection of the rotational angular momentum, $K_{\max}$. This is linked to the total number of bending mode quanta (i.e. $n_{\rm bend} = n_4 + n_5 + n_6 + n_7$) in each vibrational band. Therefore, we have a condition that

$$L_{\max} = K_{\max} \leq n_{\rm bend(max)}, \tag{2}$$

which is linked to the polyad number of equation (1). The aCeTY line list is relatively small in comparison to other polyatomic molecules of this size, largely due to the fact that the $K = L$ condition limits the number of allowed rotational sub-states in a vibrational band. As vibrational states go up quickly in energy with increasing $n_{\rm bend}$, their energy will also rise quickly with increasing values of L. We therefore do not expect high values of L to contribute until much higher energies.

TROVE uses a multistep contraction scheme. At step 1, the stretching primitive basis functions $\phi_{n_1}(\xi_1)$, $\phi_{n_2}(\xi_2)$, and $\phi_{n_3}(\xi_3)$ are generated using the Numerov–Cooley approach (Noumerov 1924; Cooley 1961; Yurchenko et al. 2007) as eigenfunctions of the corresponding 1D reduced stretching Hamiltonian operators $\hat{H}_i^{(1D)}$, obtained by freezing all other degrees of freedom at their equilibrium values in the $J = 0$ Hamiltonian. For the bending basis functions, $\phi_{n_4}(\xi_4), \ldots, \phi_{n_7}(\xi_7)$, 1D harmonic oscillators are used. These seven 1D basis sets are then combined into three sub-groups:

$$\phi_{n_1}^{(1D)}(\xi_1) = \phi_{n_1}(\xi_1), \tag{3}$$

Table 3. Extract from the .states file for the aCeTY line list. The theoretical energies were replaced with MARVEL where available (see text).

N	$\tilde{E}$	$g_{\rm tot}$	J	Unc.	$\Gamma_{\rm tot}$	n_1	n_2	n_3	n_4	n_5	n_6	n_7	$\Gamma_{\rm vib}$	K	$\tau_{\rm rot}$	$\Gamma_{\rm rot}$	$\tilde{E}^{\rm TROVE}$
68831	14.119512	21	3	0.0013	A2g	0	0	0	0	0	0	0	A1g	0	1	A2g	14.117789
68832	625.7974	21	3	0.0016	A2g	0	0	0	0	0	0	1	E1g	1	1	E1g	625.793876
68833	1242.947091	21	3	0.0011	A2g	0	0	0	0	1	0	1	E2g	2	0	E2g	1242.933977
68834	1244.544497	21	3	0.0019	A2g	0	0	0	1	0	1	0	A1g	0	1	A2g	1244.546193
68835	1463.286132	21	3	0.0014	A2g	0	0	0	0	0	0	2	A1g	0	1	A2g	1463.285595
68836	1472.462847	21	3	0.0040	A2g	0	0	0	0	1	0	1	E2g	2	0	E2g	1472.455065
68837	1865.533509	21	3	1	A2g	0	0	0	1	0	1	1	E3g	3	1	E3g	1865.740794
68838	1868.702371	21	3	0.0010	A2g	0	0	0	0	2	0	1	E1g	1	1	E1g	1868.70286
68839	1988.361458	21	3	0.1273	A2g	1	0	0	0	0	0	0	A1g	0	1	A2g	1988.353787
68840	2062.011051	21	3	0.0018	A2g	0	0	0	0	3	0	0	E1g	1	1	E1g	2062.010327
68841	2080.003537	21	3	0.0080	A2g	0	0	0	2	0	0	1	E1g	1	1	E1g	2080.003632
68842	2088.260006	21	3	0.0708	A2g	0	0	0	2	1	0	0	E3g	3	1	E3g	2088.260006
68843	2500.471967	21	3	2	A2g	0	0	0	0	2	0	2	E2g	2	0	E2g	−1
68844	2502.756348	21	3	2	A2g	0	0	0	2	0	2	0	A1g	0	1	A2g	−1
68845	2587.563753	21	3	0.0054	A2g	1	0	0	0	0	0	1	E1g	1	1	E1g	2587.571805
68846	2662.227679	21	3	0.0056	A2g	0	0	0	0	2	0	2	A1g	0	1	A2g	2662.229753
68847	2675.549505	21	3	0.5931	A2g	0	0	0	2	0	2	0	E2g	2	0	E2g	−1
68848	2699.065141	21	3	2	A2g	0	0	0	2	0	0	2	A1g	0	1	A2g	−1
68849	2703.164786	21	3	2	A2g	0	0	0	2	1	0	1	E2g	2	0	E2g	−1
68850	2894.449628	21	3	0.0033	A2g	0	0	0	4	0	0	0	A1g	0	1	A2g	2894.449274

Notes. N : State ID,
$\tilde{E}$: Term value (in cm^{-1}),
$g_{\rm tot}$: Total degeneracy,
J: Total angular momentum,
Unc: uncertainty of term value (in cm^{-1}),
$\Gamma_{\rm tot}$: Total symmetry in $\mathcal{D}_{\infty h}$(M)
n_1–n_7: TROVE vibrational quantum numbers (QN; see equation 16),
$\Gamma_{\rm vib}$: Symmetry of vibrational component of state in D$_{\infty h}$(M),
K: Projection of J on molecule-fixed z-axis ($K = L$),
$\tau_{\rm rot}$: Rotational parity (0 or 1),
$\Gamma_{\rm rot}$: Symmetry of rotational component of state in D$_{\infty h}$(M),
$\tilde{E}^{\rm TROVE}$: TROVE term value, if replaced with MARVEL (in cm^{-1}).

Table 4. Extract from a .trans file for the aCeTY line list.

f	i	A_{fi}
56645	1	2.19617648E-05
56554	1	4.23999064E-02
56923	1	3.00213998E-03
56736	1	8.28753699E-09
56839	1	8.60646693E-07
56646	1	1.25543720E-05
56555	1	8.33151532E-04
56924	1	2.58105436E-06

Notes. f: Upper state ID,
i: Lower state ID,
A_{fi}: Einstein A coefficient (in s^{-1}).

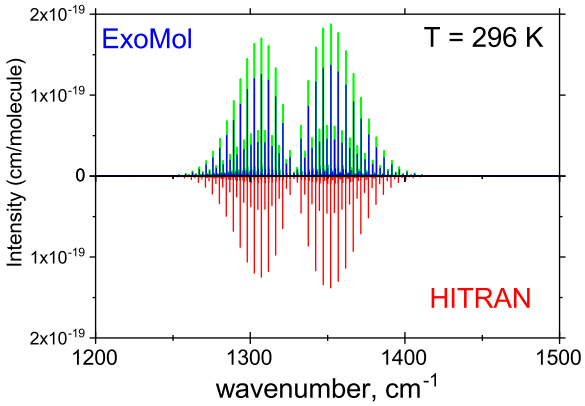

Figure 1. Comparison of aCeTY (this work) stick spectra, before (green) and after (blue) dipole moment scaling by a factor of 0.856, against HITRAN for the vibrational band (000110) Σ_u^+ of acetylene at $T = 296$ K.

$$\phi^{(2D)}_{n_2 n_3}(\xi_2, \xi_3) = \phi_{n_2}(\xi_2)\phi_{n_3}(\xi_3), \tag{4}$$

$$\phi^{(4D)}_{n_4 n_5 n_6 n_7}(\xi_4, \xi_5, \xi_6, \xi_7) = \phi_{n_4}(\xi_4)\phi_{n_5}(\xi_5)\phi_{n_6}(\xi_6)\phi_{n_7}(\xi_7), \tag{5}$$

and used to solve eigenvalue problems for the three corresponding reduced Hamiltonian operators: stretching $\hat{H}^{(1D)}$ and $\hat{H}^{(2D)}$, and bending $\hat{H}^{(4D)}$. The reduced Hamiltonians $\hat{H}^{(ND)}$ ($N = 1, 2, 4$) are constructed by averaging the total vibrational Hamiltonian operator $\hat{H}^{(J=0)}$ over the other ground vibrational basis functions (Chubb et al. 2018a,b). The eigenfunctions of the three reduced problems $\psi^{(1D)}_{\lambda_1}$, $\psi^{(2D)}_{\lambda_2}$, and $\psi^{(4D)}_{\lambda_3}$ are contracted and classified according with the $\mathcal{D}_{nh}$(M) symmetry using the symmetrisation procedure by Yurchenko et al. (2017a) to form a symmetry-adapted 7D vibrational basis set as a product $\psi^{(1D)}_{\lambda_1}\psi^{(2D)}_{\lambda_2}\psi^{(4D)}_{\lambda_3}$. At step 2, the ($J = 0$) eigenproblem is solved using this contracted basis. The eigenfunctions of the latter are then contracted again and used to form the symmetry-adapted ro-vibrational basis set, together with the spherical harmonics representing the rotational part.

For this work, the polyad number in equation (1) was chosen as $P_{\rm max} = 18$ for the primitive basis set and reduced to 16 after the first contraction. Energy cut-offs of 60 000, 50 000, and 22 000 cm^{-1}

Table 5. An extract of vibrational transition dipole moment scaling factors, $f_\mu = \sqrt{\bar{S}}$, used to produce the line list for fundamental and overtone bands. $\sqrt{\bar{S}}$ is the band intensity scaling factor. The full table is given as part of the supplementary information to this work.

Γ	υ_1	υ_2	υ_3	υ_4	l_4	υ_5	l_5	L	E_i/hc	f_μ
Π_u	0	0	0	0	0	1	1	1	730.33	1.0181
Σ_u^+	0	0	0	1	1	1	−1	0	1328.07	0.8561
Δ_u	0	0	0	1	1	1	1	2	1347.51	0.9813
Π_u	0	0	0	2	2	1	−1	1	1941.18	0.3653
Π_u	0	0	0	2	0	1	1	1	1960.87	1.3899
Π_u	0	0	0	0	0	3	1	1	2170.34	1.0429
Σ_u^+	0	0	0	3	1	1	−1	0	2560.59	1.7062
Π_u	0	1	0	0	0	1	1	1	2703.10	1.0271
Σ_u^+	0	1	0	1	1	1	−1	0	3281.91	1.0268
Σ_u^+	0	0	1	0	0	0	0	0	3294.85	0.8923
Π_u	0	1	0	2	0	1	1	1	3882.42	0.8122
Π_u	0	0	1	1	1	0	0	1	3898.34	0.5774
Π_u	1	0	0	0	0	1	1	1	4092.34	0.9985
Π_u	0	1	0	0	0	3	1	1	4140.08	0.9636
Σ_u^+	0	1	0	3	1	1	−1	0	4488.85	0.6464
Σ_u^+	0	0	1	2	0	0	0	0	4508.02	0.7419
Σ_u^+	1	0	0	1	1	1	−1	0	4673.71	1.5789
Σ_u^+	0	0	1	0	0	2	0	0	4727.07	0.8830

Table 6. An extract of the transition dipole moment scaling factors, $f_\mu = \sqrt{\bar{S}}$, used to produce the line list for hot bands starting from the (000100) Π_g state. $\sqrt{\bar{S}}$ is the band intensity scaling factor. The full table is given as part of the supplementary information to this work.

Γ	υ_1	υ_2	υ_3	υ_4	l_4	υ_5	l_5	L	E_i/hc	f_μ
Π_u	0	0	0	0	0	1	1	1	730.33	0.8730
Σ_u^+	0	0	0	1	1	1	−1	0	1328.07	1.0490
Δ_u	0	0	0	1	1	1	1	2	1347.51	1.0312
Π_u	0	0	0	2	2	1	−1	1	1941.18	0.8233
Π_u	0	0	0	2	0	1	1	1	1960.87	1.5482
Σ_u^+	0	0	0	3	1	1	−1	0	2560.59	0.5440
Δ_u	0	0	0	3	3	1	−1	2	2561.67	0.4387
Σ_u^-	0	0	0	3	1	1	−1	0	2583.84	1.3237
Π_u	0	1	0	0	0	1	1	1	2703.10	0.7272
Σ_u^+	0	0	0	1	1	3	−1	0	2757.80	1.2130
Δ_u	0	0	0	1	1	3	1	2	2773.41	1.0312
Σ_u^-	0	0	0	1	1	3	−1	0	2783.63	0.9999
Δ_u	0	0	0	1	−1	3	3	2	2796.30	1.1276
Σ_u^+	0	1	0	1	1	1	−1	0	3281.91	0.8752
Σ_u^+	0	0	1	0	0	0	0	0	3294.85	0.8065
Π_u	0	1	0	2	0	1	1	1	3882.42	1.1363
Π_u	0	0	1	1	1	0	0	1	3898.34	0.8653
Σ_u^+	1	0	0	1	1	1	−1	0	4673.71	0.9740
Σ_u^-	1	0	0	1	1	1	−1	0	4688.83	1.0084
Δ_u	1	0	0	1	1	1	1	2	4692.06	0.9710

were used for the primitive, contracted, and ($J = 0$)-contracted basis functions, respectively. The ro-vibrational basis set was formed using the energy cut-off of 22 000 cm^{-1}. The energies computed using these cut-off values are better converged than those of the *ab initio* room-temperature line list of Chubb et al. (2018b). The vibrational and rotational states are classified with the $\mathcal{D}_{nh}$ representations ($n = 34$) and the projections of the vibrational and rotational angular momenta, L and K, respectively, with the constraint $K = L$. The maximum value for the total vibrational angular momentum, $K_{max} = L_{max}$, used to build the multidimensional basis sets, see equation (2), is 16. The ro-vibrational states can only span the four irreducible representations of $\mathcal{D}_{34h}$; A_{1g}, A_{2g}, A_{1u}, and A_{2u}. For the vibrational basis set used ($L_{max} = 16$), the symmetry group $\mathcal{D}_{34h}$ is equivalent to $\mathcal{D}_{\infty h}$. The following selection rules apply to the electric dipole transitions of $^{12}C_2H_2$:

$$J' + J'' > 0 \quad \text{and} \quad J' \leftrightarrow J'' \pm 1, \tag{6}$$

$$A_{1g} \leftrightarrow A_{1u} \quad \text{and} \quad A_{2g} \leftrightarrow A_{2u}. \tag{7}$$

The corresponding nuclear statistical weights g_{ns} are 1 and 3 for the A_{1g}, A_{1u} and A_{2g}, A_{2u} pairs of states, respectively. The kinetic energy and potential energy expansions are truncated at second and eighth order, respectively (the kinetic energy terms of higher than second order appear to contribute very little to the calculated ro-vibrational energies, with expansion to higher orders becoming more computationally demanding). The equilibrium bond lengths

Table 7. Vibrational transition dipole moment scaling factors, $f_\mu = \sqrt{\bar{S}}$, used to produce the line list: hot bands starting from the (0000011) Π_u state. $\sqrt{\bar{S}}$ is the band intensity scaling factor. The full table is given as part of the supplementary information to this paper.

Γ	υ_1	υ_2	υ_3	υ_4	l_4	υ_5	l_5	L	E_i/hc	f_μ
Σ_g^+	0	0	0	2	0	0	0	0	1230.38	1.3200
Δ_g	0	0	0	2	2	0	0	2	1233.49	0.6750
Σ_g^+	0	0	0	0	0	2	0	0	1449.11	1.0060
Δ_g	0	0	0	0	0	2	2	2	1463.00	0.9773
Σ_g^+	0	1	0	0	0	0	0	0	1974.35	1.0368
Π_g	0	0	0	1	1	2	0	1	2049.06	0.8462
Π_g	0	0	0	1	−1	2	2	1	2066.97	0.7603
Π_g	0	1	0	1	1	0	0	1	2574.76	0.8972
Σ_g^+	0	0	0	2	2	2	−2	0	2648.01	0.3475
Σ_g^-	0	0	0	2	2	2	−2	0	2661.16	0.4196
Δ_g	0	0	0	2	2	2	0	2	2666.06	0.5947
Σ_g^+	0	0	0	0	0	4	0	0	2880.22	1.0651
Δ_g	0	0	0	0	0	4	2	2	2894.04	1.0543
Σ_g^+	1	0	0	0	0	0	0	0	3372.84	0.9953
Π_g	1	0	0	1	1	0	0	1	3970.05	1.5178
Π_g	0	1	0	1	1	2	0	1	4002.46	1.2100
Π_g	0	0	1	0	0	1	1	1	4016.73	0.8622
Σ_g^+	1	0	0	0	0	2	0	0	4800.13	0.9912
Δ_g	1	0	0	0	0	2	2	2	4814.19	0.9952

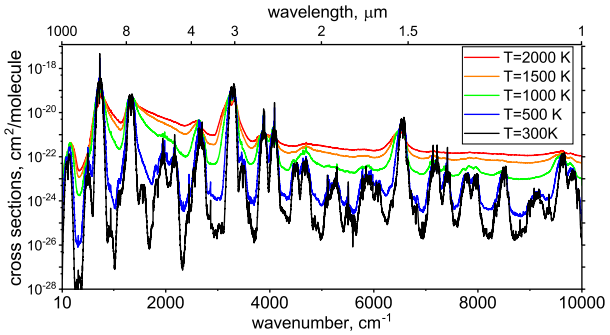

Figure 2. Variation of aCeTY line list spectra with temperature: low-resolution (1 cm^{-1}) cross-sections computed using ExoCross (Yurchenko et al. 2018). The spectrum becomes flatter with increasing temperature.

are set to 1.20498127 and 1.06295428 Å for the C–C and C–H bonds, respectively. Nuclear masses were used. Calculations were performed up to a high value of $J = 99$, which was determined by the maximum values of lower and upper energies used in the line list calculations; these have an effect on the temperature dependence of the line list, as discussed in Section 3.

2.2 Potential energy surface

TROVE represents all components of the Hamiltonian operator using a Taylor expansion about the equilibrium structure in terms of the linearized coordinates ξ_λ, $\lambda = 1 \ldots 7$ (or some 1D functions of them). This leads to a sum-of-product form that allows the the matrix to be computed as products of 1D integrals. In general, the PES, $V(\boldsymbol{\xi})$, is represented in terms of user-chosen curvilinear coordinates; TROVE uses a quadruple-precision numerical finite difference method to re-expand $V(\boldsymbol{\xi})$ in terms of the TROVE-coordinates $=\{\xi_\lambda\}$. As detailed in Chubb et al. (2018b), the TROVE linearized coordinates for C_2H_2 are selected as

$$\xi_1 = \Delta R^{\rm lin}, \quad \xi_2 = \Delta r_1^{\rm lin}, \quad \xi_3 = \Delta r_2^{\rm lin},$$
$$\xi_4 = \Delta x_1, \quad \xi_5 = \Delta y_1, \quad \xi_6 = \Delta x_2, \quad \xi_7 = \Delta y_2,$$

where $R^{\rm lin}$, $r_1^{\rm lin}$, and $r_2^{\rm lin}$ are based on the curvilinear, bond-length coordinates $R \equiv r_{\rm CC}$, $r_1 \equiv r_{\rm CH_1}$, and $r_2 \equiv r_{\rm CH_2}$; x_1, y_1, x_2, and y_2 are Cartesian coordinates of the hydrogen atoms along the x- and y-axes. The displacements are taken from the equilibrium values of R, r_1, and r_2, respectively. The equilibrium values (at the linear configuration) of x_i and y_i ($i = 1, 2$) are zero.

Here, we use the potential energy function of C_2H_2 reported recently by Chubb et al. (2018b). It is represented in terms of the linearized coordinates as follows:

$$V(\chi) = \sum_{i,j,k,\ldots} f_{ijk\ldots} \chi_1^i \chi_2^j \chi_3^k \ldots, \tag{8}$$

where χ_λ are given by

$$\chi_1 = 1 - \exp\left(-a\,\Delta R^{\rm lin}\right),$$
$$\chi_2 = 1 - \exp\left(-b\,\Delta r_1^{\rm lin}\right),$$
$$\chi_3 = 1 - \exp\left(-b\,\Delta r_2^{\rm lin}\right),$$
$$\chi_4 = \Delta x_1,$$
$$\chi_5 = \Delta y_1,$$
$$\chi_6 = \Delta x_2,$$
$$\chi_7 = \Delta y_2. \tag{9}$$

Here, a and b are two Morse parameters.

The *ab initio* PES of Chubb et al. (2018b) was computed using MOLPRO (Werner et al. 2012) at the VQZ-F12/CCSD(T)-F12c level of theory (Peterson, Adler & Werner 2008) on a grid of 66 000 points spanning the 6D nuclear-geometry coordinate space up to 50 000 cm^{-1}. A least-squares fit was used to determine the coefficients $f_{ijk\ldots}$ in equation (8) to the *ab initio* energies, using a grid of 46 986 *ab initio* points covering up to 14 000 cm^{-1}, with a weighted root-mean-square (rms) error of 3.98 cm^{-1} and an unweighted *rms* of 15.65 cm^{-1}, using 358 symmetrized parameters expanded up to eight order.

To improve the accuracy of the variational calculations, here we refine the *ab initio* PES of C_2H_2 by fitting the expansion potential parameters $f_{ijk\ldots}$ to experimental data, as outlined next.

2.3 Refinement of the potential energy surface to experimental energy levels

The refinement procedure is carried out under the assumption that the *ab initio* PES can be used to initially determine a set of energy levels and eigenfunctions. In this case, a correction is added to the *ab initio* PES in terms of a set of internal coordinates $\boldsymbol{\xi}$ (Yurchenko et al. 2011a):

$$\Delta V = \sum_{ijk\ldots} \Delta f_{ijk\ldots} \chi_1^i \chi_2^j \chi_3^k \ldots, \tag{10}$$

where $\Delta f_{ijk\ldots}$ are the refined parameters, given as correction terms to the expansion coefficients of the original PES in equation (8), with the symmetry of the molecule taken into account in the same way as for the original *ab initio* PES. The eigenfunctions of the 'unperturbed', *ab initio* Hamiltonian are used as basis functions when solving the new ro-vibrational eigenproblems with the correction ΔV to the PES included. This process is performed iteratively in TROVE, with the fitting procedure using empirical energy levels that should be added in gradually, according to the level of confidence placed in them. For details of the TROVE refinement procedure, the reader is referred to Yurchenko et al. (2011a).

Highly accurate experimentally determined data provide an essential component in the calculation of a high-quality line list, for both effective Hamiltonian and the majority of variational approaches. Fortunately for $^{12}C_2H_2$, a wealth of experimental ro-vibrational spectral data has been recorded over the decades (see, for example, Didriche & Herman 2010; Herman 2007, 2011; Amyay et al. 2016; Lyulin & Campargue 2017). Chubb et al. (2018c) gathered, collated, and analysed all such experimental data from the literature for $^{12}C_2H_2$. They used the measured active vibration–rotation energy level (MARVEL) procedure (Furtenbacher, Császár & Tennyson 2007) to provide a set of empirically derived energy levels. We use these MARVEL energies for the PES refinement procedure, with level weighted according to the level of confidence in their experimental assignment. The *ab initio* energies that were used to fit the initial PES (see above) are also included in the refinement procedure in order to constrain the shape of the refined PES to the *ab initio* PES (see Yurchenko et al. 2003).

Good QNs for acetylene states are the rotational angular momentum QN J and overall symmetry Γ. These are therefore the primary criteria used to match energy levels from the energy levels in the supplementary data of Chubb et al. (2018c) to those computed using TROVE. An important parameter in the MARVEL energy level output of Chubb et al. (2018c) is NUMTRANS, which gives the number of transitions linking a particular state to other energy levels. The higher the number of linking transitions, the higher the confidence that should be given to that empirical energy level. States with NUMTRANS = 1 were deemed unreliable and were therefore not included into the fit. A few states with NUMTRANS = 2 and large residuals were also omitted. The fact that vibrational states that include some quanta of C–H stretch are more likely to be observed in experiment than those without was used to inform our judgement when matching theoretical TROVE energy levels with their experimentally determined counterpart. Table 2 is a summary of the fit, for which only experimental energies with $J \leq 5$ were used; the *rms* errors between the experimental (MARVEL) and calculated (refined) ro-vibrational energies are shown for a set of vibrational bands in the column rms-I. The full Table is included as part of the supplementary information to this work. The vibrational QNs used for labelling the states of $^{12}C_2H_2$ in Table 2 are detailed in Table 1 together with the rotational QNs used typically (see Chubb et al. 2018c).

The refined potential energy function is available as supplementary data to this article and from exomol.com.

2.4 Band centre replacement and 'MARVELization'

As mentioned previously, TROVE uses a double layer contraction scheme with vibrational basis functions obtained as the solution of the $J = 0$ problem. This $J = 0$-representation has a more compact vibrational basis set and also facilitates the matrix elements calculations. Indeed, the vibrational part of the ro-vibrational Hamiltonian is diagonal on this basis with the matrix elements given by the corresponding vibrational ($J = 0$) band centres $E_i^{(\mathrm{vib})}$. An indirect advantage of this representation is a direct access to the $J = 0$ energies used in the consecutive ro-vibrational calculations allowing us to empirically modify the band centres (Yurchenko, Barber & Tennyson 2011b). This is a necessary procedure if the line list is to be used in any high-temperature, high-resolution Doppler-shift studies (see, for example, de Kok et al. 2014; Brogi et al. 2017), where the line positions in a line list need to be as accurate as possible. In this work, 128 calculated band centres were shifted to minimize the difference with the ro-vibrational MARVEL term value for $J \leq 5$ (Chubb et al. 2018c). Again, we only used MARVEL energies based on more than one experimental data (NUMTRANS > 1). A few NUMTRANS = 2 states represented by large residuals were suspected as outliers and also were left out. This has improved the accuracy of the resulting line positions, as demonstrated by Table 2, which shows rms errors between the experimental and calculated (refined) ro-vibrational energies for a small number of vibrational bands, before (rms-I) and after the band centre shifts (rms-II). The full Table is included as part of the supplementary information to this work. For details of the procedure see Yurchenko et al. (2011b), where it was referenced as EBSC. To improve the accuracy of our line positions, we 'MARVELize' the data: the energy levels in the ExoMol states file are replaced by the MARVEL energies of Chubb et al. (2018c). The MARVEL uncertainties are kept as part of the line list. In doing this, we take advantage of the ExoMol data format; see Tennyson, Hill & Yurchenko (2013) for details. It should be noted that the MARVEL analysis was performed in 2017, and a periodic update will be undertaken at some point in the future in order to include experimental data that has been published since then. We also provide indicative estimates of the uncertainties of all TROVE energies. This is done using the following approximation: (1) For all states, which were replaced with MARVEL energies, we take the associated MARVEL uncertainty. (2) Where we have applied band centre shifting, we take the rms error for a particular band, before band shifting (i.e. rms-I in Table 2). (3) For all other bands, which have not been 'MARVELized' or had a band centre shift applied, we use an approximate method to determine the shift, based on how the rms-I for each shifted band correlates with the number of quanta associated with the C–C stretch (n_1 in the local mode, TROVE notation), the C–H stretches ($n_2 + n_3$), and the bending modes ($n_4 + n_5 + n_6 + n_7$):

$$0.4n_2 + 0.5(n_1 + n_3) + 0.4(n_4 + n_5) + 0.003(n_4 + n_5)^2. \tag{11}$$

These uncertainities are then rounded to the nearest integer, with those under 0.5 cm^{-1} rounded up to 0.5 cm^{-1}. We stress that the estimation of these uncertainties in this way is very approximate,

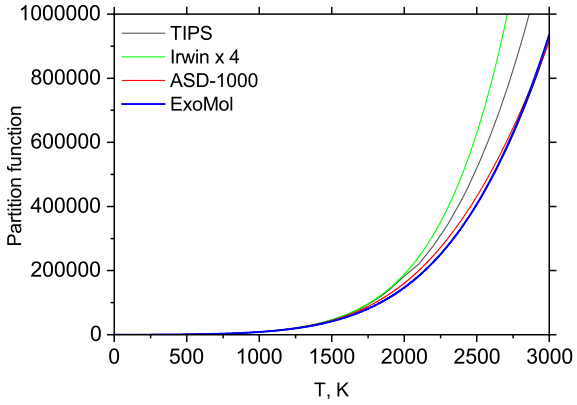

Figure 3. The $^{12}C_2H_2$ partition function up to 3000 K; comparing the states from the aCeTY line list (this work) against that computed using TIPS (Gamache et al. 2017), the coefficients of Irwin (1981), and using energies extracted from ASD-1000 (Lyulin & Perevalov 2017).

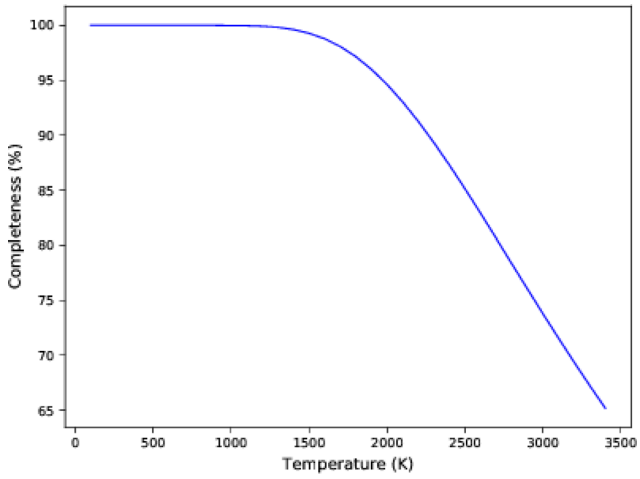

Figure 4. The completeness of the aCeTY line list as a function of temperature, up to 3400 K.

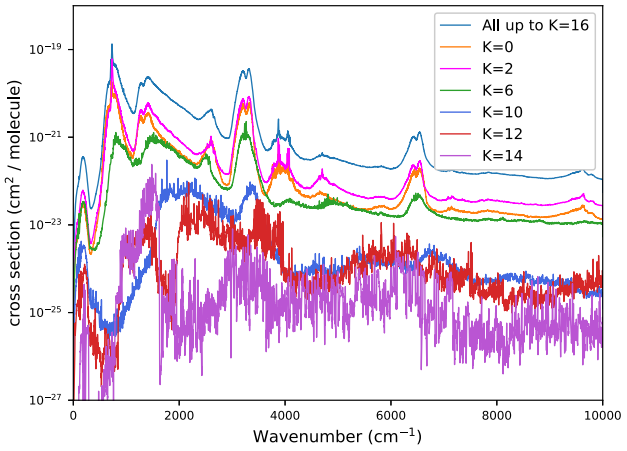

Figure 5. Contribution from transitions with upper states of different K' to the aCeTY opacity at $T = 2000$ K. Note that the $K' = 16$ transitions do not appear on this scale. The other figures appear to be cited in the correct order.

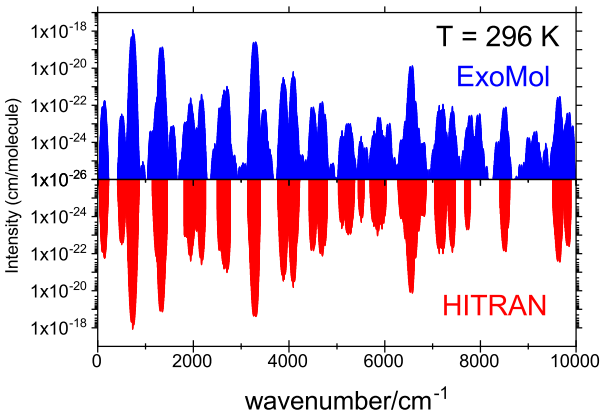

Figure 6. Comparison of the aCeTY stick spectrum with the HITRAN data for the range up to 10 000 cm^{-1} at 296 K.

and the main aim is to distinguish between those states considered reliable and those states that should not be considered reliable when comparing to high-resolution observations. Tables 3 and 4 give extracts from the aCeTY line line in ExoMol format.

2.5 Dipole moment surface

Here, we use the *ab initio* DMS computed by Chubb et al. (2018b) with the finite field method in MOLPRO at the CCSD(T)/aug-cc-PVQZ level of theory on a grid of 66 000 points covering energies up to 50 000 cm^{-1}. The electric dipole moment components, μ_α ($\alpha = x, y, z$), were represented using the same set of seven linearized coordinates as for the $3N - 5$ potential above to the following function:

$$\mu_x(\zeta) = \sum_i F^x_{ijk\ldots} \zeta_1^i \zeta_2^j \zeta_3^k \ldots, \tag{12}$$

$$\mu_y(\zeta) = \sum_i F^y_{ijk\ldots} \zeta_1^i \zeta_2^j \zeta_3^k \ldots, \tag{13}$$

$$\mu_z(\zeta) = \sum_i F^z_{ijk\ldots} \zeta_1^i \zeta_2^j \zeta_3^k \ldots. \tag{14}$$

where ζ_λ are given by

$$\zeta_1 = \Delta R^{\rm lin}, \quad \zeta_2 = \Delta r_1^{\rm lin}, \quad \zeta_3 = \Delta r_2^{\rm lin},$$
$$\zeta_4 = \Delta x_1, \quad \zeta_5 = \Delta y_1, \quad \zeta_6 = \Delta x_2, \quad \zeta_7 = \Delta y_2.$$

Use was made of discrete symmetries (see Chubb et al. 2018a), and the three components of the dipole were expanded up to seventh order and symmetrized according to the operations of $\mathcal{D}_{12h}$. The value of n here in $\mathcal{D}_{nh}$ is determined by the order up to which the function (dipole moment or potential energy) is expanded. See, for example, Chubb (2018). The three Cartesian components of the dipole moment, μ_x, μ_y, μ_z, transform differently to one another (μ_x and μ_y as E_{1u} and μ_z as A_{2u} for $D_{nh}(M)$ (Bunker & Jensen 2006)): the μ_x and μ_y components share the corresponding expansion parameters, while that the parameters for the μ_z component are independent. This dipole moment function is provided as supplementary material to this work as a Fortran program.

2.6 Vibrational transition dipole moment scaling

In order to improve the quality of the line intensities, at least for the vibrational bands known experimentally from HITRAN, we

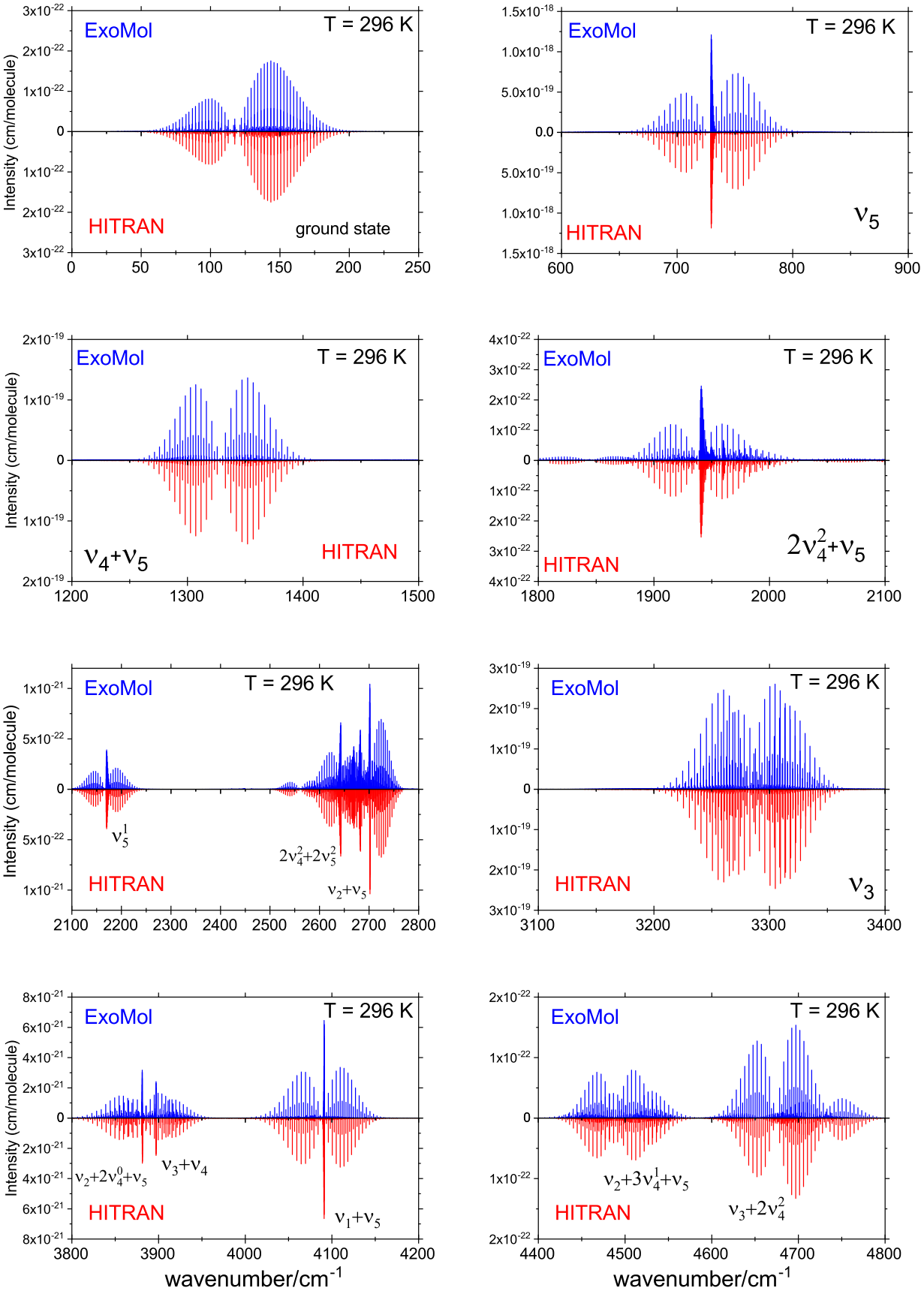

Figure 7. Comparison of the aCeTY stick spectra (with scaling of the dipole moment applied) against HITRAN for different vibrational bands of acetylene at 296 K (in the range 0–5000 cm^{-1}). The vibrational assignment of the strongest bands is shown.

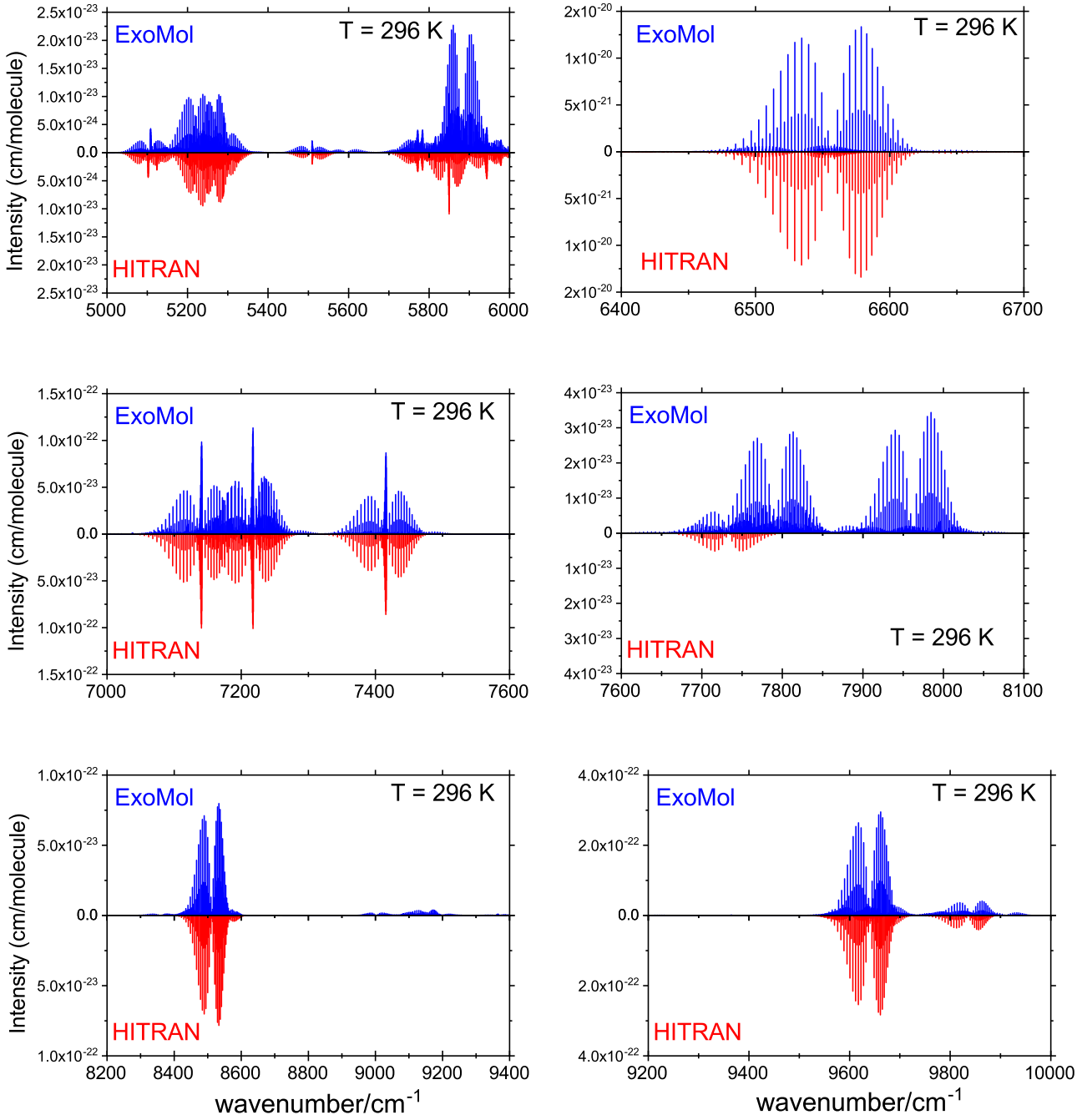

Figure 8. Comparison of the aCeTY stick spectra against HITRAN (with scaling of the dipole moment applied) against HITRAN for different vibrational bands of acetylene at 296 K (in the range 5000–10 000 cm^{-1}).

have applied scalings to the corresponding vibrational transition dipole moments. This is a new approach implemented in TROVE that takes advantage of the $J = 0$ representation of the basis set. Since the rovibrational line intensities are computed using vibrational matrix elements of the electronically averaged dipole moment components $\bar{\mu}_x$, $\bar{\mu}_y$, and $\bar{\mu}_z$, modifying these vibrational moments by a scaling factor specific for a given band will propagate this scaling to all rotational lines within this band in a consistent manner. A band scaling factor was obtained as a geometric average of n matched individual line intensities within each vibrational band:

$$\bar{S} = \left[\prod_{i=1}^{n} \frac{I_i^{\text{HITRAN}}}{I_i^{\text{TROVE}}}\right]^{\frac{1}{n}}, \tag{15}$$

which leads to a $\sqrt{\bar{S}}$ scaling factor on the dipole moment. To this end, we have correlated the HITRAN transition $T = 296$ K intensities to the corresponding intensities computed with TROVE using the methodology described above (after the band centre shifts).

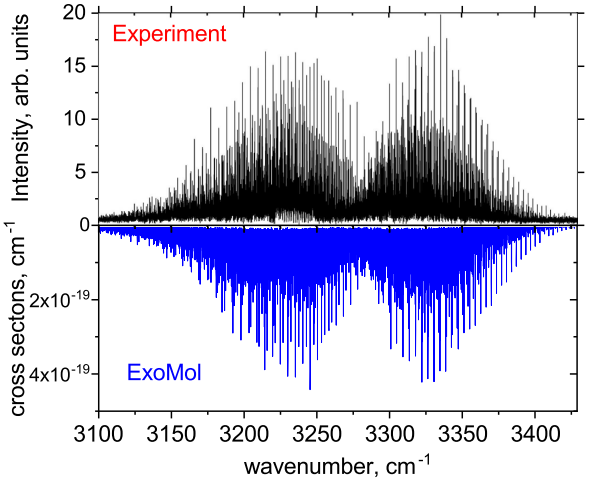

Figure 9. Comparison of the acetylene spectra in the 3 μm region computed using aCeTY at $T = 1355$ K with the experimental data of Amyay et al. (2009). The aCeTY cross-sections were generated using ExoCross and a Voigt line profile assuming $P = 1$ atm.

Fig. 1 shows an example of the dipole scaling procedure applied to the (000110) Σ_u^+ band. The unscaled TROVE intensities (shown in green) are ∼1.365 times stronger than those from HITRAN, at 296 K. We can therefore apply a 0.856 ($= 1/\sqrt{1.365}$) scaling factor to the z dipole moment component of the corresponding vibrational matrix element $\langle 000110|\mu_z|000000\rangle$, with the result shown in Fig. 1 in blue. We have thus applied scaling factors to 216 bands, listed in the supplementary information to this work. Extracts are given in Tables 5–7.

3 RESULTS: THE ACETY LINE LIST

The aCeTY line list has been computed using the variational calculations outlined above. Fig. 2 illustrates the temperature dependence of the acetylene spectra computed using the aCeTY line list, with cross-sections computed using ExoCross (Yurchenko, Al-Refaie & Tennyson 2018) at a variety of temperatures between 300 and 2000 K. The cross-sections are calculated at a low resolution of 1 cm^{-1} for demonstration purposes.

The TROVE assignment is based on the largest basis set contribution to the eigenfunction. TROVE uses the local mode QNs to assign vibrational state, collected in Table 1. This selection of the QNs is based on the choice of the vibrational basis set in equations (3)–(5). There is no direct correlation between the local mode and normal mode assignment. For an approximation correlation, the following rules apply:

$$\upsilon_1 + \upsilon_3 = n_2 + n_3, \tag{16}$$

$$\upsilon_2 = n_1, \tag{17}$$

$$\upsilon_4 + \upsilon_5 = n_4 + n_5 + n_6 + n_7. \tag{18}$$

The number density of a particular molecular state as a fraction of the total number density of the molecular species is given by the Boltzmann law. The total internal partition function, Q, is a sum over all molecular states, weighting each by their probability of occupation at a given temperature, and therefore offers an indication of the completeness of a calculated line list at a particular

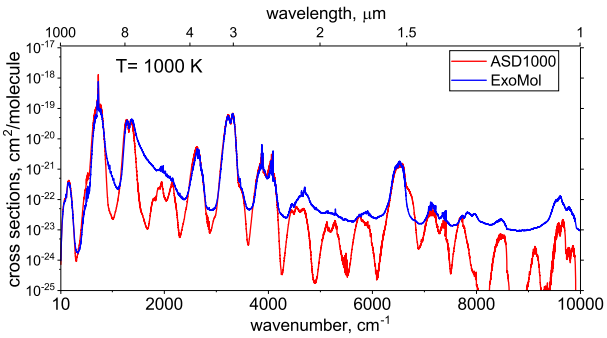

Figure 10. Comparison of the aCeTY line list with ASD-1000 (Lyulin & Perevalov 2017); spectra computed up to 10 000 cm^{-1} at 1000 K.

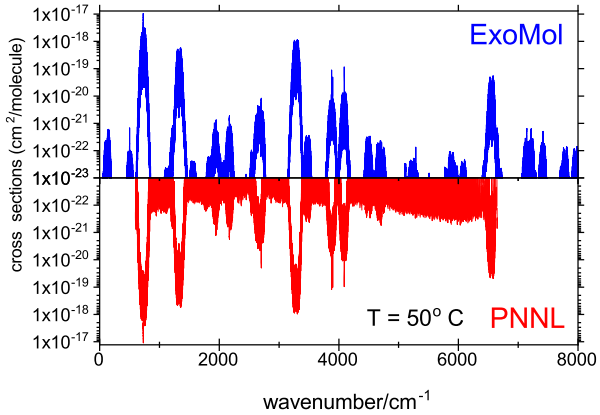

Figure 11. Comparison of the aCeTY cross-sections against PNNL (Sharpe et al. 2004) at $T = 50°$. The aCeTY cross-sections were generated using the Gaussian line profile with half width at half-maximum of 0.01 cm^{-1}. The PNNL data below 1×10^{-22} cm^2 /molecule are largely due to noise.

temperature:

$$Q = \sum_{i=1}^{N} {g_{ns}}^{(i)}(2J_i + 1)\exp\left(\frac{-c_2\tilde{E}_i}{T}\right). \tag{19}$$

Here, $c_2 = \frac{hc}{k}$ is the second radiative constant, $\tilde{E}_i$ is the energy term value of each i molecular state (relative to the ground ro-vibronic state), T is the temperature, ${g_{ns}}^{(i)}$ is the nuclear statistical weight of each i molecular state, and the sum is over all molecular states. The partition function can easily be computed from the ExoMol states file (Tennyson et al. 2016) using ExoCross (Yurchenko et al. 2018). A comparison of the partition function for $^{12}C_2H_2$ computed using the aCeTY states file against the partition function computed using TIPS (Gamache et al. 2017), the coefficients by Irwin (1981), and the energies extracted from the ASD-1000 data base of Lyulin & Perevalov (2017) is given in Fig. 3. All these partition functions, with the exception of the one due to Irwin (1981), use the 'physicists' convention that weights ortho and para states of $^{12}C_2H_2$ 3 and 1, respectively, as opposed to the weighting of 0.75 and 0.25 often adopted by astronomers.

The temperature at which a line list is complete up to is generally dictated by the range of energy levels included in a line list production. For the aCeTY line list, we use a maximum lower energy of 12 000 cm^{-1}, and a maximum upper energy of 22 000 cm^{-1}, which gives a line list that is complete up to 10 000 cm^{-1} (i.e. $\lambda > 1$ μm), i.e. the maximum upper energy is 10 000 cm^{-1} above the maximum lower energy level value. The completeness as a function

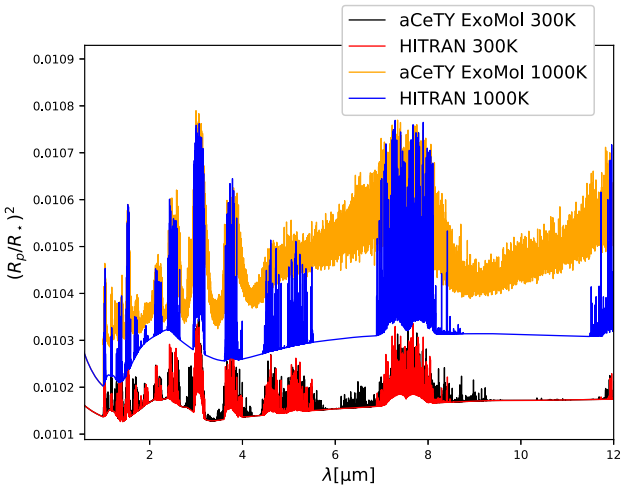

Figure 12. The transmission spectra of a hypothetical planetary atmosphere of a Jupiter-size planet around a solar-like star, with an atmosphere of pure $^{12}C_2H_2$, at 1000 K, computed using TAU-REX (Waldmann et al. 2015). A comparison is made using aCeTY (this work) against HITRAN line list data as input into the cross-sections used in the transmission spectrum computation.

of temperature of such a line list can be estimated by calculating the partition function up to the lower energy level cut-off as a percentage of the total partition function that includes all states involved in a line list calculation. Fig. 4 gives these values at a variety of temperatures. A line list is generally considered to be 'complete' if the ratio of the partition function of the lower energy states to the partition function of all energy states involved in a line list calculation is > 90 per cent. It can be seen from Fig. 4 that the aCeTY line list is therefore estimated, using this metric, to be complete up to around 2200 K. The other factor that could have an impact on the completeness of the line list is the value used for $K_{max} = L_{max}$ in equation (2). As discussed, however, we do not expect the states below 22 000 cm^{-1} which are being used for the line list to have high values of L_{max}; the bending states that correspond to a high value of L are expected at very high energies, and therefore temperatures. Fig. 5 shows the contributions from transitions with upper states with different values of K (=L) to a line list computed up to $K_{max} = L_{max} = 16$. It can be seen that states with higher values of K contribute a vanishingly small amount to the overall opacity. We therefore do not expect increasing the value of $K_{max} = L_{max}$ in a calculation to have a significant effect on the opacity of a acetylene even at high temperatures.

A complete description of the ExoMol data structure along with examples was reported by Tennyson et al. (2016). The ExoMol .states file contains all computed ro-vibrational energies (in cm^{-1}) relative to the ground state. Each energy level is assigned a unique state ID with symmetry and QN labelling; an extract for $^{12}C_2H_2$ is shown in Table 3. The .trans files, which are split into frequency windows for ease of use, contain all computed transitions with upper and lower state ID labels, and Einstein A coefficients. An example from a .trans file for the aCeTY line list is given in Table 4.

4 COMPARISON TO OTHER DATA

Fig. 6 shows an overview of an absorption spectrum of $^{12}C_2H_2$ computed using aCeTY (this work) to that produced using HITRAN-2016 (Gordon et al. 2017) at $T = 296$ K for the wavenumber range from 0 to 10 000 cm^{-1}. Apart from some missing weak bands in HITRAN, it shows a generally good agreement. Figs 7 and 8 give more detailed comparisons of the main bands of $^{12}C_2H_2$ in the range 0–10 000 cm^{-1} with the data from HITRAN-2016 (Gordon et al. 2017), again in the form of stick spectra (absorption coefficients) at room-temperature. The overall agreement of the line positions and intensities is good, except several weaker bands of C_2H_2, overestimated by aCeTY, as well as bands not present in HITRAN. Table 2 gives a summary of the accuracy of the line positions for $J \leq 5$ states presented in MARVEL and used in the refinement and band centre corrections. The full table is given as supplementary information to this work.

Fig. 9 shows the hot spectrum (cross-sections) of the 3 μm band of C_2H_2 at $T = 1355$ K compared to the experimental data by Amyay et al. (2009) demonstrating the generally good agreement also at high temperatures.

The ASD-1000 data base of Lyulin & Perevalov (2017) is a calculated acetylene line list, which covers transitions up 10 000 cm^{-1} and $J = 100$, based on the use of an effective Hamiltonian fit to experimental data and extrapolated to higher energies. The energies and intensities at room temperature agree reasonably well with those in the HITRAN-2016 (Gordon et al. 2017) data base (see Lyulin & Perevalov 2017) and Lyulin & Campargue 2017 for detailed comparisons), and ASD-1000 has been used to update the 2016 HITRAN release in the low-energy region (Gordon et al. 2017; Jacquemart, Lyulin & Perevalov 2017). Fig. 10 gives a comparison of cross-sections computed using the aCeTY and ASD-1000 line lists at $T = 1000$ K. The results are significantly different, and it would appear that ASD-1000 fails to adequately account for the many hot bands that become important at higher temperatures.

A comparison with PNNL is given in Fig. 11, for $T = 50°$.

5 EXOPLANET ATMOSPHERES

Fig. 12 gives the transmission spectra of a hypothetical planetary atmosphere of a Jupiter-size planet around a solar-like star, with an atmosphere of pure $^{12}C_2H_2$, at 1000 K, computed using TAU-REX (Waldmann et al. 2015). A comparison of such an atmosphere using the aCeTY line list is made against one using HITRAN cross-section data (both are computed at a resolving power of $R = \lambda/\Delta\lambda = 10\,000$). It can be seen that a large amount of opacity would be lost if one used HITRAN data at high temperatures. This is further demonstrated by an atmosphere of a planet with the same mass and temperature, which contains H_2O (Polyansky et al. 2018), CO_2 (Rothman et al. 2010a), CH_4 (Yurchenko et al. 2017b), CO (Li et al. 2015), HCN (Barber et al. 2014), H_2S (Azzam et al. 2016), and C_2H_2 at abundances representative of a carbon-dominated atmosphere. Fig. 13 shows the differences between using aCeTY and HITRAN data as input into the transmission spectrum computation for C_2H_2. Low-resolution ($R = \lambda/\Delta\lambda = 300$) k-tables are used here. All other molecules and parameters remain the same between the two spectra. The cross-sections and k-tables (the latter are produced using a method of opacity sampling that enables low-resolution computations while still taking strong opacity fluctuations at high resolution into account; see, for example, Min 2017) used in these model will shortly be made publicly available (Chubb et al. 2020).

6 SUMMARY AND FUTURE WORK

In this work, we present a new ro-vibrational line list for the ground electronic state of the main isotopologue of acetylene, $^{12}C_2H_2$; the aCeTY line list. This line list was computed as part of the

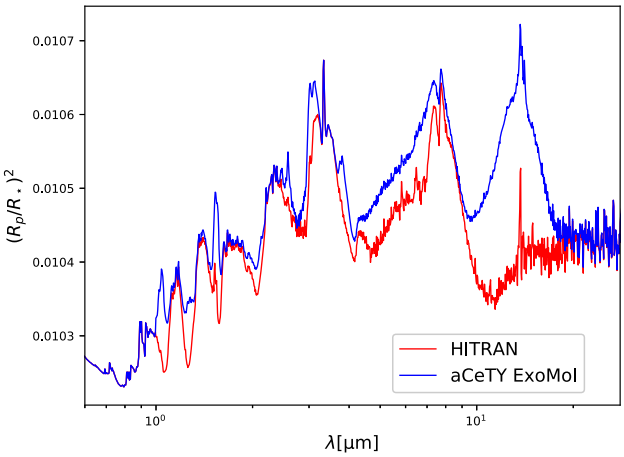

Figure 13. The transmission spectra of a hypothetical planetary atmosphere of a Jupiter-size planet around a solar-like star, with an atmosphere of H_2O, CO_2, CH_4, CO, HCN, H_2S, and C_2H_2 at abundances representative of a carbon-dominated atmosphere at 1000 K, computed using TAU-REX (Waldmann et al. 2015). A comparison is made using aCeTY (this work) against HITRAN line list data as input into the transmission spectrum computation for C_2H_2. All other molecules and parameters remain the same between the two spectra.

ExoMol project (Tennyson & Yurchenko 2012; Tennyson et al. 2016), for characterizing exoplanet and cool stellar atmospheres. It is considered complete up to 2200 K, with transitions computed up to 10 000 cm^{-1} (down to 1 μm), with lower and upper energy levels up to 12 000 and 22 000 cm^{-1} considered, respectively. The calculations were performed up to a maximum value for the vibrational angular momentum, $K_{max} = L_{max} = 16$, and maximum rotational angular momentum, $J = 99$. The aCeTY line list is based on *ab initio* electronic structure calculations for the potential energy and DMSs, but with improvements on the accuracy of both the line positions and the dipole moments made using the wealth of experimental data available from the literature.

Comparisons against other available line list data demonstrate that the aCeTY line list is the most complete and accurate available line list for acetylene to date. It is therefore recommended for use in characterizing exoplanet and cool stellar atmospheres. Computing cross-section and k-table opacity data for $^{12}C_2H_2$, at a range of temperatures and pressures suitable for use in exoplanet atmospheres, for use in retrieval codes such as TAU-REX (Waldmann et al. 2015), ARCIS (Min et al. 2020), NEMESIS (Irwin et al. 2008), and PETITRADTRANS (Molliére et al. 2019) will be published soon in Chubb et al. (2020).

For high-resolution applications, however, some caution is advised. More work needs to be done, which is ongoing, to further improve and ensure the accuracy of line position to achieve precision required for studies of exoplanets using high-resolution Doppler spectroscopy. The line list can be improved by augmenting the MARVEL analysis of Chubb et al. (2018c) with new laboratory data, such as Twagirayezu, Hall & Sears (2018), Di Sarno et al. (2019), Nürnberg et al. (2019), and then inserting the resulting energy levels in aCeTY; this would ensure that energies and associated transition wavenumbers are at the current limit of accuracy. The high-accuracy experiments of Tao et al. (2018) and Liu et al. (2013; which was not included in Chubb et al. 2018c) demonstrates that updates should be made to the $\nu_1 + 3\nu_3$ band included in the MARVEL analysis of $^{12}C_2H_2$.

The new intensity scaling technique presented in this work will be useful for future high-precision spectroscopic applications, especially if combined with the MARVELization procedure. It has the potential to target the accuracy of experiment when predicting line intensities within a given vibrational band at different temperatures.

The line lists aCeTY can be downloaded from the CDS, via ftp://cdsarc.u-strasbg.fr/pub/cats/J/MNRAS/, or http://cdsarc.u-strasbg.fr/viz-bin/qcat?J/MNRAS/, or from www.exomol.com.

ACKNOWLEDGEMENTS

This work was supported by the UK Science and Technology Research Council (STFC) No. ST/R000476/1 and through a studentship to KLC. This work made extensive use of UCL's Legion high performance computing facility along with the STFC DiRAC HPC facility supported by BIS National E-infrastructure capital grant ST/J005673/1 and STFC grants ST/H008586/1 and ST/K00333X/1. KLC acknowledges funding from the European Union's Horizon 2020 Research and Innovation Programme, under grant 776403.

REFERENCES

Al-Refaie A. F., Polyansky O. L., Ovsyannikov R. I., Tennyson J., Yurchenko S. N., 2016, MNRAS, 461, 1012
Amyay B. et al., 2009, J. Chem. Phys., 131, 114301
Amyay B., Fayt A., Herman M., Auwera J. V., 2016, J. Phys. Chem. Ref. Data, 45, 023103
Aringer B., Girardi L., Nowotny W., Marigo P., Lederer M. T., 2009, A&A, 503, 913
Azzam A. A. A., Tennyson J., Yurchenko S. N., Naumenko O. V., 2016, MNRAS, 460, 4063
Ba Y. A. et al., 2013, J. Quant. Spectrosc. Radiat. Transfer, 130, 62
Bains W., 2004, Astrobiology, 4, 137
Barber R. J., Strange J. K., Hill C., Polyansky O. L., Mellau G. C., Yurchenko S. N., Tennyson J., 2014, MNRAS, 437, 1828
Belay N., Daniels L., 1987, Appl. Environ. Microbiol., 53, 1604
Bilger C., Rimmer P., Helling C., 2013, MNRAS, 435, 1888
Brogi M., Line M., Bean J., Désert J.-M., Schwarz H., 2017, ApJ, 839, L2
Brooke T. Y., Tokunaga A. T., Weaver H. A., Crovisier J., BockeleeMorvan D., Crisp D., 1996, Nature, 383, 606
Bunker P. R., Jensen P., 2006, Molecular Symmetry and Spectroscopy, 2nd edn. NRC Research Press, Ottawa, Canada
Cassady S. J., Peng W. Y., Hanson R. K., 2018, J. Quant. Spectrosc. Radiat. Transfer, 221, 172
Cernicharo J., 2004, ApJ, 608, L41
Chubb K. L., 2018, PhD thesis, Univ. College London
Chubb K. L., Jensen P., Yurchenko S. N., 2018a, Symmetry, 10, 137
Chubb K. L., Yachmenev A., Tennyson J., Yurchenko S. N., 2018b, J. Chem. Phys., 149, 014101
Chubb K. L. et al., 2018c, J. Quant. Spectrosc. Radiat. Transfer, 204, 42
Chubb K. L. et al., 2020, A&A
Coles P. A., Yurchenko S. N., Tennyson J., 2019, MNRAS, 490, 4638
Cooley J. W., 1961, Math. Comp., 15, 363
de Graauw T. et al., 1997, A&A, 321, L13
de Kok R. J., Birkby J., Brogi M., Schwarz H., Albrecht S., de Mooij E. J. W., Snellen I. A. G., 2014, A&A, 561, A150
Dhanoa H., Rawlings J. M. C., 2014, MNRAS, 440, 1786
Didriche K., Herman M., 2010, Chem. Phys. Lett., 496, 1
Dinelli B. M. et al., 2019, Icarus, 331, 83
Di Sarno V. et al., 2019, Optica, 6, 436
Drossart P., Bézard B., Atreya S., Lacy J., Serabyn E., Tokunaga A., Encrenaz T., 1986, Icarus, 66, 610
Encrenaz T., Combes M., Atreya S. K., Romani P. N., Fricke K., 1986, A&A, 162, 317

Endres C. P., Schlemmer S., Schilke P., Stutzki J., Müller H. S. P., 2016, J. Mol. Spectrosc., 327, 95
Furtenbacher T., Császár A. G., Tennyson J., 2007, J. Mol. Spectrosc., 245, 115
Gamache R. R. et al., 2017, J. Quant. Spectrosc. Radiat. Transfer, 203, 70
Gaudi B. S. et al., 2017, Nature, 546, 514
Gautschy-Loidl R., Höfner S., Jørgensen U. G., Hron J., 2004, A&A, 422, 289
Gaydon A., 2012, The Spectroscopy of Flames. Springer Science Business Media B.V. 1974, Springer Netherlands
Goebel J. H., Bregman J. D., Strecker D. W., Witteborn F. C., Erickson E. F., 1978, ApJ, 222, L129
Gordon I. E. et al., 2017, J. Quant. Spectrosc. Radiat. Transfer, 203, 3
Herman M., 2007, Mol. Phys., 105, 2217
Herman M., 2011, High-resolution Infrared Spectroscopy of Acetylene: Theoretical Background and Research Trends. Wiley, New York, p. 1993
Hörst S. M., 2017, J. Geophys. Res., 122, 432
Hughes E. E., Gorden R., 1959, Anal. Chem., 31, 94
Irwin A. W., 1981, ApJS, 45, 621
Irwin P. G. J. et al., 2008, J. Quant. Spectrosc. Radiat. Transfer, 109, 1136
Jacquemart D., Lyulin O., Perevalov V. I., 2017, J. Quant. Spectrosc. Radiat. Transfer, 203, 440
Jacquinet-Husson N. et al., 2016, J. Mol. Spectrosc., 327, 31
Jørgensen U. G., Hron J., Loidl R., 2000, A&A, 356, 253
Kelly M. W., Richley J. C., Western C. M., Ashfold M. N. R., Mankelevich Y. A., 2012, J. Phys. Chem. A, 116, 9431
Lahuis F. et al., 2005, ApJ, 636, L145
Lederer M. T., Aringer B., 2009, A&A, 494, 403
Le Roy L. et al., 2015, A&A, 583, A1
Li G., Gordon I. E., Rothman L. S., Tan Y., Hu S.-M., Kassi S., Campargue A., Medvedev E. S., 2015, ApJS, 216, 15
Liu A.-W., Li X.-F., Wang J., Lu Y., Cheng C.-F., Sun Y. R., Hu S.-M., 2013, J. Chem. Phys., 138, 014312
Loidl R., Höfner S., Jørgensen U. G., Aringer B., 1999, A&A, 342, 531
Lovett R. A., 2011, Enceladus Named Sweetest Spot for Alien Life, Nature. Springer Nature
Lyulin O. M., Campargue A., 2017, J. Quant. Spectrosc. Radiat. Transfer, 203, 461
Lyulin O. M., Campargue A., 2018, J. Quant. Spectrosc. Radiat. Transfer, 215, 51
Lyulin O. M., Perevalov V. I., 2017, J. Quant. Spectrosc. Radiat. Transfer, 201, 94
Lyulin O. M., Béguier S., Hu S. M., Campargue A., 2018, J. Quant. Spectrosc. Radiat. Transfer, 208, 179
Lyulin O., Vasilchenko S., Mondelain D., Campargue A., 2019, J. Quant. Spectrosc. Radiat. Transfer, 234, 147
Madhusudhan N., Agúndez M., Moses J. I., Hu Y., 2016, Space Sci. Rev., 205, 285
Mant B. P., Yachmenev A., Tennyson J., Yurchenko S. N., 2018, MNRAS, 478, 3220
Marigo P., Aringer B., 2009, A&A, 508, 1539
Matsuura M. et al., 2006, MNRAS, 371, 415
McKay C. P., Smith H. D., 2005, Icarus, 178, 274
McKemmish L. K., Yurchenko S. N., Tennyson J., 2016, MNRAS, 463, 771
Metsälä M., Schmidt F. M., Skytta M., Vaittinen O., Halonen L., 2010, J. Breath Res., 4, 046003
Mikhailenko S. N., Babikov Y. L., F. G. V., 2005, Atmos. Ocean. Opt., 18, 685
Miller L. G., Baesman S. M., Oremland R. S., 2014, AGU Fall Meeting Abstracts, p. P53B–4009
Min M., 2017, A&A, 607, A9
Min M., Ormel C. W., Chubb K. L., Helling C., Kawashima Y., 2020, A&A, (In Press)
Mollière P., Wardenier J. P., van Boekel R., Henning T., Molaverdikhani K., Snellen I. A. G., 2019, A&A, 627, A67
Moses J. I., Bézard B., Lellouch E., Gladstone G. R., Feuchtgruber H., Allen M., 2000, Icarus, 143, 244
Noumerov B. V., 1924, MNRAS, 84, 592
Nürnberg J., Alfieri C. G. E., Chen Z., Waldburger D., Picqué N., Keller U., 2019, Opt. Express, 27, 3190
Oppenheimer B. R. et al., 2013, ApJ, 768, 24
Oremland R. S., Voytek M. A., 2008, Astrobiology, 8, 45
Owens A., Yachmenev A., Thiel W., Tennyson J., Yurchenko S. N., 2017, MNRAS, 471, 5025
Peterson K. A., Adler T. B., Werner H.-J., 2008, J. Chem. Phys., 128, 084102
Polyansky O. L., Kyuberis A. A., Lodi L., Tennyson J., Yurchenko S. N., Ovsyannikov R. I., Zobov N. F., 2017, MNRAS, 466, 1363
Polyansky O. L., Kyuberis A. A., Zobov N. F., Tennyson J., Yurchenko S. N., Lodi L., 2018, MNRAS, 480, 2597
Rangwala N. et al., 2018, ApJ, 856, 9
Rey M., Nikitin A. V., Babikov Y. L., Tyuterev V. G., 2016, J. Mol. Spectrosc., 327, 138
Ridgway S. T., 1974, ApJ, 187, L41
Ridgway S. T., Hall D. N. B., Wojslaw R. S., Kleinmann S. G., Weinberger D. A., 1976, Nature, 264, 345
Rinsland C. P., Baldacci A., Rao K. N., 1982, ApJS, 49, 487
Rothman L. S. et al., 2010a, J. Quant. Spectrosc. Radiat. Transfer, 111, 2139
Rothman L. S. et al., 2010b, J. Quant. Spectrosc. Radiat. Transfer, 111, 2139
Schmidt F. M., Vaittinen O., Metsälä M., Kraus P., Halonen L., 2010, Appl. Phys. B, 101, 671
Seager S., Bains W., Hu R., 2013, ApJ, 775, 104
Shabram M., Fortney J. J., Greene T. P., Freedman R. S., 2011, ApJ, 727, 65
Sharpe S. W., Johnson T. J., Sams R. L., Chu P. M., Rhoderick G. C., Johnson P. A., 2004, Appl. Spectrosc., 58, 1452
Singh S. et al., 2016, ApJ, 828, 55
Sousa-Silva C., Al-Refaie A. F., Tennyson J., Yurchenko S. N., 2015, MNRAS, 446, 2337
Tanaka M., Letip A., Nishimaki Y., Yamamuro T., Motohara K., Miyata T., Aoki W., 2007, PASJ, 59, 939
Tao L.-G., Hua T.-P., Sun Y. R., Wang J., Liu A.-W., Hu S.-M., 2018, J. Quant. Spectrosc. Radiat. Transfer, 210, 111
Tennyson J., Yurchenko S. N., 2012, MNRAS, 425, 21
Tennyson J., Yurchenko S. N., 2016, Exp. Astron., 40, 563
Tennyson J., Yurchenko S. N., 2017, Mol. Astrophys., 8, 1
Tennyson J., Hill C., Yurchenko S. N., 2013, in AIP Conf. Proc. Vol. 1545, 6th International Conference on Atomic and Molecular Data and Their Applications ICAMDATA-2012. Am. Inst. Phys., New York, p. 186
Tennyson J. et al., 2016, J. Mol. Spectrosc., 327, 73
Tsiaras A. et al., 2016, ApJ, 820, 99
Tsuji T., 1986, ARA&A, 24, 89
Twagirayezu S., Hall G. E., Sears T. J., 2018, J. Chem. Phys., 149, 154308
Underwood D. S., Tennyson J., Yurchenko S. N., Huang X., Schwenke D. W., Lee T. J., Clausen S., Fateev A., 2016a, MNRAS, 459, 3890
Underwood D. S., Tennyson J., Yurchenko S. N., Clausen S., Fateev A., 2016b, MNRAS, 462, 4300
van Dishoeck E. F., Wright C. M., Cernicharo J., González-Alfonso E., de Graauw T., Helmich F. P., Vandenbussche B., 1998, ApJ, 502, L173
Waite J. H. et al., 2006, Science, 311, 1419
Waldmann I. P., Tinetti G., Rocchetto M., Barton E. J., Yurchenko S. N., Tennyson J., 2015, ApJ, 802, 107
Watson J. K. G., 1968, Mol. Phys., 15, 479
Werner H.-J., Knowles P. J., Knizia G., Manby F. R., Schütz M., 2012, WIREs Comput. Mol. Sci., 2, 242
Yachmenev A., Yurchenko S. N., 2015, J. Chem. Phys., 143, 014105
Yurchenko S. N., Tennyson J., 2014, MNRAS, 440, 1649
Yurchenko S. N., Carvajal M., Jensen P., Herregodts F., Huet T. R., 2003, Chem. Phys., 290, 59
Yurchenko S. N., Thiel W., Jensen P., 2007, J. Mol. Spectrosc., 245, 126
Yurchenko S. N., Barber R. J., Tennyson J., Thiel W., Jensen P., 2011a, J. Mol. Spectrosc., 268, 123
Yurchenko S. N., Barber R. J., Tennyson J., 2011b, MNRAS, 413, 1828

Yurchenko S. N., Tennyson J., Bailey J., Hollis M. D. J., Tinetti G., 2014, Proc. Nat. Acad. Sci., 111, 9379
Yurchenko S. N., Yachmenev A., Ovsyannikov R. I., 2017a, J. Chem. Theory Comput., 13, 4368
Yurchenko S. N., Amundsen D. S., Tennyson J., Waldmann I. P., 2017b, A&A, 605, A95
Yurchenko S. N., Al-Refaie A. F., Tennyson J., 2018, A&A, 614, A131
Zak E. J., Tennyson J., Polyansky O. L., Lodi L., Zobov N. F., Tashkun S. A., Perevalov V. I., 2017, J. Quant. Spectrosc. Radiat. Transfer, 189, 267

SUPPORTING INFORMATION

Supplementary data are available at *MNRAS* online.

Table 2. An extract of the Obs.-Calc. residuals for $^{12}C_2H_2$.
Table 5. An extract of vibrational transition dipole moment scaling factors, $f_\mu = \sqrt{\bar{S}}$, used to produce the line list for fundamental and overtone bands.
Table 6. An extract of the transition dipole moment scaling factors, $f_\mu = \sqrt{\bar{S}}$, used to produce the line list for hot bands starting from the (000100) Π_g state.
Table 7. Vibrational transition dipole moment scaling factors, $f_\mu = \sqrt{\bar{S}}$, used to produce the line list: hot bands starting from the (0000011) Πu state.
Table S1. The full table of vibrational transition dipole moment scaling factors, $f_\mu = \sqrt{\bar{S}}$, used to produce the line list for remaining hot bands.

Please note: Oxford University Press is not responsible for the content or functionality of any supporting materials supplied by the authors. Any queries (other than missing material) should be directed to the corresponding author for the article.

This paper has been typeset from a TEX/LATEX file prepared by the author.